Supporting Information

S1. Simulations

As the contact angle deviates from $\theta_c=90°$, the interface distortion created by an anisotropic particle increases, and the capillary interaction energy also increases. For any particle geometry with up-down symmetry, the capillary energy E is symmetric with respect to the condition of indifferent wetting, i.e. changing the contact angle from $90°+\varepsilon$ to $90°-\varepsilon$ leaves the magnitude of E unaltered. This property must result in a quadratic dependence of E on $|90°-\theta_c|$, for $|90°-\theta_c|<<1$. This dependence is demonstrated for ellipsoids in Fig. S1, and for cylinders in Fig. S2, for $\theta_c<90°$.

The elastic constants G and κ, which characterized the elastic response of chains of side-by-side ellipsoids (see Sections 3.1 and 3.4). are proportional to the curvature of the energy profile for $\phi=180°$. Comparison of Fig. 7 (a) in the paper with similar plots in Refs. [1, 2] shows that the plot of E vs. bond angle is independent of θ_c, as far as the overall shape of the energy profile is concerned. Owing to the similarity of these profiles, a quadratic dependence of G and κ on $|90°-\theta_c|$ thus holds approximately.
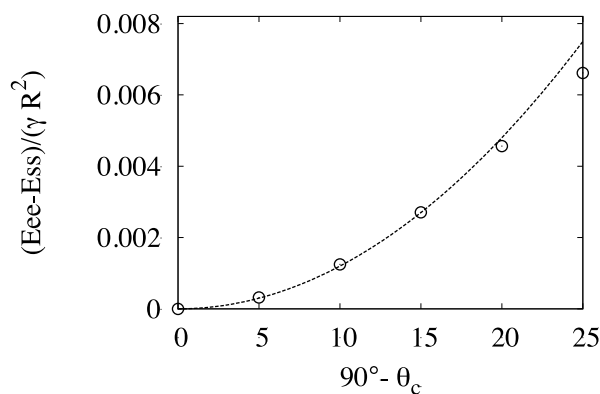

Fig. S1 Capillary energy difference $E_{ee}-E_{ss}$ between ellipsoids in contact in end-to-end and side-to-side configurations vs. contact angle deviation with respect to 90°. The dashed line is the function $1.2\text{x}10^{-5}\text{x}(90°-\theta_c)^2$
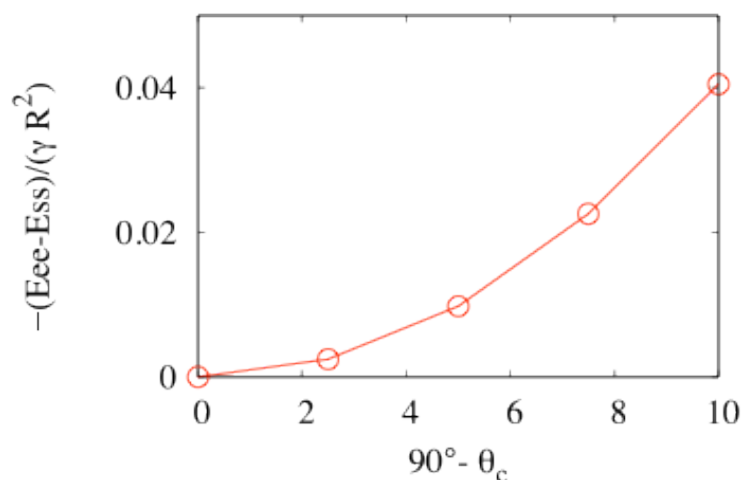
Fig. S2 Capillary energy difference $E_{ee}-E_{ss}$ between cylinders ($\eta=120, d=0.45$) in end-to-end and side-to-side configurations vs. contact angle deviation with respect to 90°.

The amplitude of the interfacial distortion induced by isolated ellipsoids increases with aspect ratio [2, 3]. The energy difference between the end-to-end and side-to-side configurations also increase with Λ [2]. The amplitude of the interface distortion induced by isolated cylinders instead decreases, although weakly, with increasing Λ [4]. To illustrate the effect of aspect ratio on the capillary interaction energy in the case of cylinders we show in Table S2 the total capillary energy for different combinations of surface-to-surface separation and aspect ratios, comparing the end-to-end and the side-to-side configurations. It can be seen that the energy difference between side-to-side and end-to-end is always positive, and increases with aspect ratio for a given value of d. The trend for the dependence of the capillary energy on Λ is therefore analogous to that observed in the case of ellipsoids. Energy differences are expected to saturate to an asymptotic value for $\Lambda \gg 1$, a limit not considered in this work.

End-to-end	$\Lambda=2.5$	$\Lambda=3.0$	$\Lambda=3.5$
d=0.45R	1586.391447	1583.825301	1581.258428
d=0.60R	1586.403052	1583.837090	1581.270441

Side-to-side	$\Lambda=2.5$	$\Lambda=3.0$	$\Lambda=3.5$
d=0.45R	1586.410872	1583.845546	1581.279682
d=0.60R	1586.421499	1583.847940	1581.281642

Difference	$\Lambda=2.5$	$\Lambda=3.0$	$\Lambda=3.5$
d=0.45R	0.019425	0.020245	0.021254
d=0.60R	0.018447	0.010850	0.011201

Table S1. Values of the total surface energy for each cylinder in a pair, for different combinations of d and Λ. In these simulations, the contact angle is 80° and η is set to 120, corresponding to cylinders with sharp edges. The total capillary interaction energy is equal to twice the numerical value reported in each field.
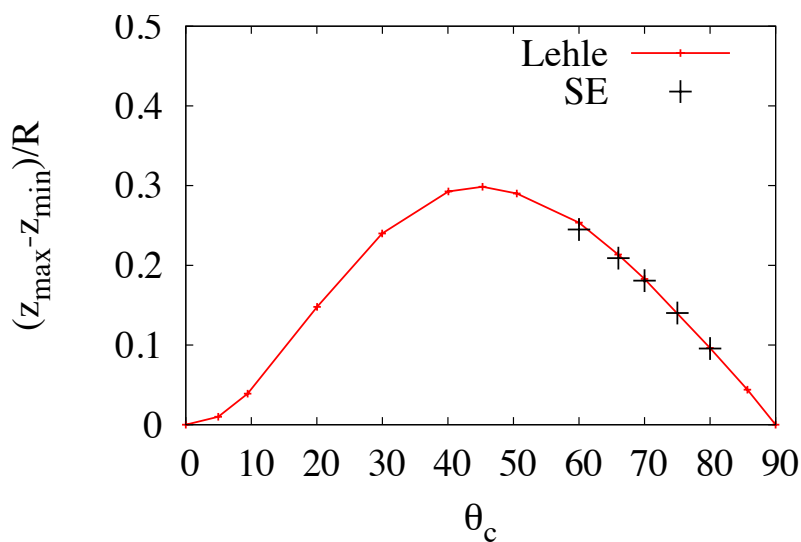

Fig. S3: Maximum contact line difference vs. contact angle for isolated ellipsoids, comparing Surface Evolver simulations data with those of Ref. [3], in which the numerical method assumed small slopes. The aspect ratio is 5.

Figure S3 shows a comparison of the maximum amplitude of the contact line distortion at the contact line for an isolated ellipsoid of aspect ratio equal to 5. The red line with symbols shows data reproduced from Fig. 4 in Ref. [3], where results based on the numerical solution of the *linearized* Young-Laplace equation were reported. The black crosses indicate results obtained by us, with Surface Evolver, for selected contact angles. The two simulation methods give practically identical results for contact angles close to 90°, while small differences, which we attribute to non-linear effects that are not captured in Lehle's method (and in Loudet's method of Refs. [1] and [2]), are discernable for θ_c=66° and 60°. These small differences can be important, since the energy depends quite strongly on the amplitude of the deformation (quadratically in the superposition limit).
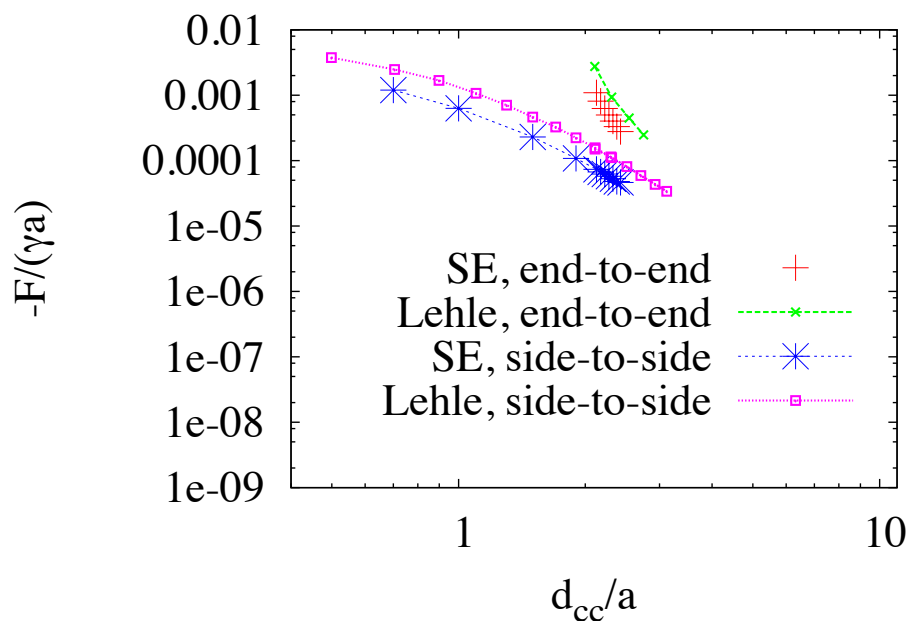
Fig. S4: Capillary force vs. center-to-center separation, comparing Surface Evolver simulation results (SE) with those of Ref. [3]. The aspect ratio is 5 and the contact angle θ_c=66°.

Fig. S4 shows the attractive force for selected values of the center-to-center separation d_{cc}, comparing our results with those published in Ref. [3]. The Surface Evolver simulation gives smaller value than those given by the approximate simulation based on the linear Young-Laplace equation (which is not totally unexpected in view of the results presented in Fig. S3). The results given by the two simulations are comparable in order of magnitude and overall trend. Although these results potentially indicate the importance of non-linear effects not captured in the simulations of Refs. [1,2,3], further studies are needed to ascertain the limits of validity of linear approximations; for a meaningful comparison, these studies should include information about the numerical convergence properties of the adopted scheme.

References

1.   *Loudet, J.C. and B. Pouligny, Self-assembled capillary arrows. Epl, 2009. **85(2)**.*

2.   *Loudet, J.C. and B. Pouligny, How do mosquito eggs self-assemble on the water surface? European Physical Journal E, 2011. **34**(8).*

3.   *Lehle, H., E. Noruzifar, and M. Oettel, Ellipsoidal particles at fluid interfaces. European Physical Journal E, 2008. **26**(1-2): p. 151-160.*

4.   *Lewandowski, E.P., Cavallaro, M., Botto, L., Bernate, J. C., Garbin, V., Stebe, and K. J., Orientation and Self-Assembly of Cylindrical Particles by Anisotropic Capillary Interactions. Langmuir, 2010, 26 (19), p. 15142–15154.*

S2. Experiment

S2.1. Non-magnetic microparticles fabrication

Non-magnetic cylindrical microparticles (diameter 4.5 µm, length 10 µm) were fabricated using standard photolithography [2]. Briefly, a negative photoresist (SU-8 2010, MicroChem Corp.) was deposited onto a silicon wafer (Montco Silicon) by spin-coating at 3000 RPM for 30 s. The photoresist was then exposed to UV light (365nm) through a photomask, and subsequently developed. The resulting cylindrical microposts were then released from the wafer by sonication of the entire wafer in ethanol, producing cylinders with well-defined features. The contact angle of SU-8 with the air-water interface is 80˚ [2], as measured by optical tensiometer (Theta Tensiometer, KSV Instrument).

S2.2. Magnetic microparticles fabrication

Magnetic micro-cylinders were fabricated by sputtering 99.99% pure nickel metal (ACI Alloys Inc.) into lithographically-defined wells. A silicon wafer was sputtered with a 100 nm-thin copper sacrificial film. A layer of positive photoresist (SPR 220-7.0, MicroChem Corp.) was then deposited at 2250 RPM for 30 s and soft-baked at 115 °C for 60 s. The photoresist was exposed to UV light (365nm) through the same photomask used to fabricate the non-magnetic particles, and developed. This process gave cylindrical "holes" in a layer of positive photoresist. Nickel was then sputtered onto the wafer. The positive photoresist was dissolved by acetone, thus removing the nickel film. The Ni particles were released from the wafer by etching away the copper film.

The Ni particles were 5 µm in diameter and 10 µm in length, as determined by optical

microscopy (Zeiss Imager, M1m, Carl Zeiss Inc). The contact angle of Ni with the air-water interface was measured to be 82˚. Prior to their release, the Ni cylinders were exposed to a strong magnetic field (B=3411 G, Neodymium block magnet, BY0X06-N52, K&J Magnetics) parallel to the cylinder axis to magnetize the particles. The resulting magnetic properties of the released cylinders were characterized by applying a small magnetic field (B = 20 G) to isolated particles trapped at the air-water interface. The cylinders aligned with their axis parallel to applied field. When field direction was rapidly flipped, the cylinder axis rotated through 180 degrees to follow the field, indicating that the particles indeed possessed a permanent magnetic dipole moment parallel to the cylinder axis. From the rate of rotation, which was dictated by a balance of the magnetic torque on the cylinders and the known viscous drag torque, as described in Ref. [7], the magnetic moment of the cylinders was determined to be approximately $\mu = 1 \times 10^{-10}$ emu.

S2.3. Chain formation

A very dilute (0.1% by weight) mixture of Ni and SU-8 cylinders (ratio 1:5) was spread to an air-water interface. The dispersion was prepared by mixing the particles in a 1:9 v/v isopropanol/deionized-water solvent mixture. About 30 to 50 µL of dispersion was used in each experiment. After spreading, time was allowed for the alcohol component of the solvent to evaporate. Since Ni and SU-8 have similar contact angles, several chains of SU-8 cylinders with incorporated Ni cylinders formed spontaneously by capillary self-assembly. We studied chains containing a single Ni cylinder and several SU-8 cylinders. The mixture was sufficiently dilute that magnetic or capillary interactions between distant chains could be neglected.

S2.4. Bond-Bending Experiments

Experiments to characterize the bending strength of the cylinder capillary bond were performed by rotating chains at the air-water interface and hence subjecting them to magnetic and viscous torques. Isolated chains of SU-8 cylinders with incorporated magnetic cylinders were set into

rotation and their motion monitored using an inverted optical microscope with *in situ* magnetic field, as described in Ref. [7]. Briefly, two sets of four computer-controlled electromagnetic coils positioned symmetrically above and below the microscope focal plane, which was coincident with the air-water interface, created magnetic fields with prescribed profiles in the microscope field of view. First, profiles with weak magnetic-field gradients were employed to translate a chain into the field of view. Then, a uniform field of constant magnitude B rotating in the focal plane at constant angular velocity ω was applied. In steady state, the low-Reynolds-number environment dictated that the chain rotated in response to the field with the Ni cylinder's magnetic moment vector, and hence the chain axis, lagging the field by an angle q such that the magnetic torque and the drag torque from the fluid T_{drag} balanced,

$$T_{drag} = \mu B \sin\theta, \qquad (0.1)$$

where $T_{drag} = \zeta_r \omega$ and ζ_r is the rotational drag coefficient of the chain. We estimate the drag coefficient as $\zeta_r = \alpha \zeta_b$, where ζ_b is the bulk rotational drag coefficient of a cylinder having length equal to that of the chain and α is the area fraction of the chain immersed in water. A similar approach was used in Ref. [2]. For ζ_b we use the semi-empirical expression [4]

$$\zeta_b = \frac{\pi \eta_0 L^3}{3\left(\ln p + C_r\right)}$$

where η_0 is the dynamic viscosity of water at 20 °C, L and p are the chain length and aspect ratio, respectively, and $C_r = -0.662 + 0.917/p - 0.050/p^2$. The value of α was estimated from simulations of isolated cylinders to be about 60% [2].

In the measurements, B was held fixed at a large value ($B = 80$ G) and ω was increased in steps to increase the drag torque and hence the bending torque. The maximum achievable ω and thus the maximum torque was attained for $\theta = 90°$. For larger rotation rates, the chain failed to follow the external magnetic field and instead exhibited a more complicated rotational trajectory In the four-cylinder chain experiment shown in Fig. 2 of the paper, the maximum rotation rate was 7.4Hz. For R=2.25 μm, L=40 μm, and ω = 7.4Hz the rotational drag, and thus the maximum torque supported by each capillary bond, is calculated to be

$$T_{drag} = 2.8 \times 10^5 \, kT \tag{0.1}.$$

As mentioned in the paper, at this rotation rate the bonds displayed no measurable bending. Given the precision of the video tracking of the rotating chains, we estimate that bending angles greater than 2 degrees would be resolvable. Measurements on other chains gave similar results.

S2.6. Monolayer of chains

To form a dense monolayer of cylindrical micro-particles (Fig. 1(b) in the paper), we performed sequential spreading of a 10% by weight suspension of SU-8 particles onto the air-water interface in a Langmuir trough (Nima Technology). At least 20 minutes elapsed between each deposition to allow for solvent evaporation. In each injection, 2-3 ml of particle-solvent mixture were added. At a surface coverage of approximately 20%, a percolating network formed by capillarity. We then quasi-statically compressed the interface in steps of 4 cm^2 at a rate of 1.0 cm^2/min until a packed monolayer formed. At least 10 minutes elapsed between successive compressions to allow for monolayer relaxation to occur.

References

(1)   Badaire, S., Cottin-Bizonne, C., Woody, J. W., Yang, A., and Stroock, A. D. *J. Am. Chem. Soc.* **2007**, *129*, 40–41.

(2)   Lewandowski, E. P., Bernate, J. A., Searson, P. C., and Stebe, K. J. *Langmuir* **2008**, *24*, 9302–9307.

(3)   Lapointe, C. P., Reich, D. H., and Leheny, R. L. *Langmuir* **2008**, *24*, 11175–11181.

(4)   Ortega, A. and de la Torre, G. J. *J. Chem. Phys.* **2003**, *119*, 9914.

(5)   Tirado, M. M., Martínez, C. L., de la Torre, G. J. *J. Chem. Phys.* **1984**, *81*, 2047.

(6)   Kunesh, J. G., Brenner, H., O'Neill, M. E., and Falade, A. *J. Fluid Mech.* **1985**, *154*, 29.

(7)   Lee, M. H., Lapointe, C. P., Reich, D. H., Stebe, K. J., and Leheny, R. L. *Langmuir* **2009**, *25*, 7976–7982.

(8)   Anguelouch, A., Leheny, R. L., and Reich, D. H. *Appl. Phys. Lett.* **2006**, *89*,

111914.

(9)   McNaughton, B.H., Kehbein, K.A., Anker, J.N., and Kopelman, R., J. Phys. Chem. B, **2006**, (110), 18958-18964.